Experimental and Computational Multiphase Flow
Vol. 3, No. 3, 2021, 171–185
https://doi.org/10.1007/s42757-020-0084-5

Multi-fluid modelling of bubbly channel flows with an adaptive multi-group population balance method

D. Papoulias[1] (✉), A. Vichansky[2], M. Tandon[3]

1. Siemens Industries Software Computational Dynamics Ltd., 200 Shepherds Bush Road, London, W6 7NL, UK
2. Siemens Industries Software Computational Dynamics Ltd., Basil Hill Road, Didcot, OX11 7HJ, UK
3. Siemens Industries Software (India) Pvt.Ltd., Global Business Park Mehrauli–Gurgaon Road, Gurgaon, 122002, India

Abstract

Mass, momentum, and energy transfer in bubbly flows strongly depends on the bubble's size distribution, which determines the contact area between the interacting phases. Characterization of bubble sizes in polydisperse flows requires empirical modelling of sub-grid physical mechanisms such as break-up and coalescence. In the present work an adaptive multiple size-group (A-MuSiG) method is incorporated into the Eulerian multiphase solver available in Simcenter STAR-CCM+ in order to model polydisperse bubbly flows in horizontal and vertical channels. The disperse phase-space is discretized into multiple size-groups each represented by its own size, number-density, and velocity field. The diameter of the bubbles in each of the size-groups varies in time and space, dynamically adapting to the local flow conditions. The interphase momentum transfer between the continuous phase and polydisperse bubbles is modelled through drag, virtual mass, turbulent dispersion, and lift forces. For modelling sub-grid bubble break-up and coalescence processes, different phenomenological kernels are evaluated. The empirical parameters of the adopted kernels are calibrated in two steps. The initial stage of the analysis considers experimental channel flows at low Reynolds number and zero-gravity conditions, under which the bubble size distribution is solely dependent on coalescence. As part of the second phase of the evaluation, additional parametric simulations in turbulent channel flows are performed in order to calibrate the break-up models, assuming the coalescence scaling constants derived in the previous step. The obtained results demonstrate that in flows with high turbulent mixing the ensuing bubble dynamics are strongly coupled to the internal properties of the population, which in turn influence the developing multiphase interactions in a transient manner.

Keywords

adaptive population balance model
turbulent break-up
coalescence
bubbly channel flow

Article History

Received: 30 March 2020
Revised: 23 June 2020
Accepted: 19 August 2020

Research Article

1 Introduction

A frequent assumption adopted in two-fluid solvers for modelling multiphase flows with droplets and bubbles is that the dispersed phase population is monodispersed, therefore consisting of particles of the same size. In this manner, the interaction length-scale is treated as a constant, which implies that the problem can be effectively simplified into a set of continuous and dispersed Eulerian flow-fields representing the main flow characteristics, e.g., mass, momentum, and energy. This approach provides robust and useful solutions for many applications; however, the particle length-scales encountered in multiphase flows can vary significantly due to different physical processes, in which case the hypothesis of monodispersed interactions is not representative of the physics. The modelling limitations associated with a constant particle size can be lifted by introducing additional population balance equations (PBEs), accounting for the conservation of the internal properties of dispersed populations such as number of particles, mass, or volume (Ramkrishna, 2000). In principle, the discretization of particle population properties by means of PBE is analogous to the statistical description of mechanical and thermodynamic fluid systems, realized by the classical Liouville's and Boltzmann's equations respectively (Bird, 1976). In this way, PBEs can provide an extension to the macroscopic physical modelling of Eulerian multiphase

The original version of this article was revised due to a retrospective Open Access order.

✉ dimitrios.papoulias@siemens.com

models by bridging information for particle processes that is perceivable at a microscale level. Knowledge of how microscopic processes influence the evolution of population characteristics of dispersed systems in time and space is crucial for a wide range of industrial and scientific fields involved in research relating to particle mechanisms such as nucleation, breakage and coalescence, aggregation and crystallization growth (Ramkrishna, 2014).

The numerical methods developed for the solution of PBEs can be generally classified into three categories: the stochastic Monte-Carlo technique (MC) (Zhao et. al., 2007), method of moments (MoM) (Randolph, 1964; Frenklach, 2002), and method of classes (Kumar and Ramkrishna, 1996a; Bhole et. al., 2008). Amongst these methods, the MC seems to be the most suitable approach for modelling population balances of discrete Lagrangian particles. However, despite the recent progress (Bartsch et al., 2019), stochastic predictions can be extensively expensive for large samples of particle clusters and prone to intrinsic noise due to statistical errors (Hao et al., 2013), what is ill-suited to deterministic CFD. Among the deterministic methods the MoM is perceived as the most computationally efficient option that can be tailored to cover a diverse range of multiphase applications (Randolph and Larson, 1971; Sajjadi et al., 2012; Shu et al., 2012). Since an equation for a low-order moment contains some higher-order moments, a closure strategy is typically needed in order to terminate the otherwise infinite chain of equations. For bubbly flows with coalescence and break-up effects, the MoM usually accounts for only a small set of low-order moments for the bubble size distribution (BSD) (number of the bubbles, surface area, volume, etc.), which is sufficient for reconstructing the variance and mean size of dispersed population given a predefined distribution shape (Lo and Zhang, 2009). Similarly, the MoM can be converted into a set of ordinary differential equations for describing the particle's number-density decay in Brownian coagulation of aerosols, by assuming a priori a logarithmic distribution for the dispersed population as well as simplifying the relevant collision kernel to manageable expansion terms (Lee et al., 1984; Wang et al., 2019). The quadrature method of moments (QMoM) (McGraw, 1997) employs the product-difference algorithm (Gordon, 1968) in order to reconstruct the BSD from the finite set of moments, while the direct quadrature method of moments (DQMoM) (Marchisio and Fox, 2005) solves directly for the quadrature points. Note that the QMoM method requires solution of an eigenvalue problem, whilst the DQMoM inverts an ill-conditioned matrix, both strategies severely affecting the computational cost and robustness of the methods. An alternative approach for modelling the population distribution is pursued in the method of classes, also known as multiple size-group method (MuSiG), where the particle distribution is discretized into different size-groups each represented by its own flow properties. However, since the population distribution is not known a priori, a large number of fixed classes are typically required for discretizing the spectrum of sizes in the phase-space. For this reason, the computational cost associated with the method of classes can be prohibitively high. The limitations associated with the fixed discretization approach for the phase-space are addressed by developing adaptive techniques that account for the variations of the size range. By dynamically adjusting the discretization elements/classes to follow the size evolution of the population, the moving pivot (Kumar and Ramkrishna, 1996b) and moving sectional methods (Kim and Seinfeld, 1990; Mohs and Bowman, 2011) are successful in modelling condensation/evaporation of droplets in aerosols as well as coagulation, nucleation, surface growth, and agglomeration in particulate flows, while preserving meaningful characteristics for the distribution shape. A conceptually similar adaptive discretization algorithm, the adaptive MuSiG method (A-MuSiG) is developed in Simcenter STAR-CCM+ (Vikhansky and Splawski, 2015; Vikhansky, 2017). The method employs the direct quadrature spanning tree algorithm (Vikhansky, 2013) in order to calculate the volume fraction and the number density of each size-group; this allows each class to adaptively follow the development of the population sizes in the phase-space, as a result of physical mechanisms such as break-up and coalescence.

In principle, break-up and coalescence models are derived in view of different sub-grid particle mechanisms, relating to isotropic turbulence–particle interactions (Tsouris and Tavlarides, 1994; Martinez-Bazan et al., 2010), bubble–bubble collisions and film-formation (Luo, 1993), as well as viscous forces and surface instabilities (Kocamustafaogullari and Ishii, 1995). To a degree, the available models are established based on scaling features of turbulence (Hinze, 1955) while usually and due to the empiricism involved, the efficiency of the underlying physical processes is further calibrated according to experiments. In the current analysis, the A-MuSiG method is evaluated in bubbly channel flows for different empirical coalescence and break-up kernels, as well as closures for modelling bubble interactions and turbulence. The bubble coalescence efficiency is calibrated using a zero-gravity experiment (Kamp et al., 2001) and likewise the break-up model is tuned using available spatial BSD measurements in horizontal pipe flows (Kocamustafaogullari and Wang, 1991). The A-MuSiG model is further validated against experiments in vertical channel flows past an obstacle (Krepper et al., 2009). Special attention is given to the performance of the A-MuSiG method due to its adaptive algorithm.

2 Multi-group population balance model

In the context of the Eulerian multiphase models, multifluid

flow-fields are represented by continuous and dispersed phases which coexist in space and time as interpenetrating continua. In order to account for polydispersed bubble populations, the dispersed phase-space is partitioned into M size-groups, each one modelled with its own set of conservation equations. The size-groups are allowed to interact with the surrounding continuous flow via the acting forces as well as with each other through coalescence and break-up events. Accordingly, bubble break-up events transport mass and momentum to the smaller group-sizes, while the opposite occurs when bubbles coalesce and thus move to classes with larger sizes. Details regarding the numerical algorithm of the A-MuSiG model can be found in published work (Vikhansky and Splawski, 2015), while for the purposes of the current study the basic formulation is presented.

In the case of an isothermal flow without phase-change effects, the Reynolds-averaged (RA: $\langle\cdot\rangle$) mass conservation for group i of the dispersed phase is expressed as

$$\frac{\partial \rho_{\mathrm{p}} \overline{\alpha}_i}{\partial t} + \nabla \cdot \left(\rho_{\mathrm{p}} \overline{\alpha}_i \left\langle \boldsymbol{u}_i \right\rangle_i \right) = m_{ij} - m_{ji} \tag{1}$$

where ρ_{p} is the density of the dispersed bubbles, $\overline{\alpha}_i$ is the RA volume-fraction, m_{ij} is the mass flux between groups i and j due to breakage and coalescence, and $\langle \boldsymbol{u}_i \rangle$ is the phase-averaged velocity:

$$\left\langle \boldsymbol{u}_i \right\rangle_i = \frac{\left\langle \alpha_i \boldsymbol{u}_i \right\rangle}{\overline{\alpha}_i} \tag{2}$$

The flow velocity of bubbles in group-size i is given by the momentum conservation law:

$$\frac{\partial \rho_{\mathrm{p}} \overline{\alpha}_i \left\langle \boldsymbol{u}_i \right\rangle_i}{\partial t} + \nabla \cdot \left(\rho_{\mathrm{p}} \overline{\alpha}_i \left\langle \boldsymbol{u}_i \right\rangle_i \left\langle \boldsymbol{u}_i \right\rangle_i \right) = - \overline{\alpha}_i \nabla p - \nabla \cdot \overline{\boldsymbol{\tau}}_i + \left\langle \Sigma \boldsymbol{F}_i \right\rangle + m_{ij} \left\langle \boldsymbol{u}_j \right\rangle_j - m_{ji} \left\langle \boldsymbol{u}_i \right\rangle_i \tag{3}$$

The terms in the RHS of Eq. (2) are the pressure-gradient (∇p), the Reynolds stresses ($\overline{\boldsymbol{\tau}}_i$), the phase interaction forces ($\boldsymbol{F}_i$), and inter-group momentum transfer due to break-up and coalescence.

Coupling between the continuous and dispersed phases is achieved by integrating relevant interaction forces acting on bubbles. In particular, the implemented bubble force balance is modelled as follows:

$$\Sigma \boldsymbol{F} = \boldsymbol{F}_{\mathrm{B}} + \boldsymbol{F}_{\mathrm{D}} + \boldsymbol{F}_{\mathrm{VM}} + \boldsymbol{F}_{\mathrm{TD}} + \boldsymbol{F}_{\mathrm{L}} + \boldsymbol{F}_{\mathrm{T}} \tag{4}$$

The resultant particle force postulated in Eq. (3) consists of contributions due to buoyancy ($\boldsymbol{F}_{\mathrm{B}}$), drag ($\boldsymbol{F}_{\mathrm{D}}$), virtual-mass ($\boldsymbol{F}_{\mathrm{VM}}$), turbulent dispersion ($\boldsymbol{F}_{\mathrm{TD}}$), lift ($\boldsymbol{F}_{\mathrm{L}}$), as well as turbophoresis ($\boldsymbol{F}_{\mathrm{T}}$) effects. The necessary force closures for the drag and virtual-mass forces are adopted from established models in the literature (Auton et al., 1988; Tomiyama et al., 2002). For the lift coefficient a constant value is assumed ($C_{\mathrm{L}} = 0.1$). The turbulent dispersion force is a direct product of the Reynolds averaging procedure, involving covariance terms between the volume-fraction, velocity, and acceleration of the continuous phase. The closure model of these extra terms is derived based on the Boussinesq gradient hypothesis:

$$\boldsymbol{F}_{\mathrm{TD}} = -\rho_{\mathrm{p}} \overline{\alpha}_i D_{\mathrm{T}} \left(\frac{\nabla \overline{\alpha}_i}{\overline{\alpha}_i} - \frac{\nabla \overline{\alpha}_{\mathrm{c}}}{\overline{\alpha}_{\mathrm{c}}} \right) \left(\frac{1}{\tau_{\mathrm{D},i}} \right) \tag{5}$$

where D_{T} is the turbulent diffusion coefficient assumed to be directly analogous to the corresponding eddy diffusivity of the continuous phase (Hinze, 1959), and $\tau_{\mathrm{D},i}$ is the relaxation time of the particles that belong to group i. Bubble dispersion is further augmented by turbophoresis effects. As a result, particles responding to turbulent fluctuations are reorganized inside the flow-field (Young and Leeming, 1997), which for bubbles implies migration towards areas of high turbulence. The closure model for this additional stress-term is formulated as

$$\boldsymbol{F}_{\mathrm{T}} = -\rho_{\mathrm{c}} \overline{\alpha}_i C_{\mathrm{VM}} \left(\frac{\nabla \overline{\alpha}_{\mathrm{c}}}{\overline{\alpha}_{\mathrm{c}}} \left\langle \boldsymbol{\tau}_{\mathrm{c}}^n \right\rangle - \frac{\nabla \overline{\alpha}_i}{\overline{\alpha}_i} \left\langle \boldsymbol{\tau}_i^n \right\rangle \right) \tag{6}$$

where C_{VM} denotes the virtual-mass coefficient and $\boldsymbol{\tau}^n$ is the nth component of the Reynolds stress tensor.

The approach pursued for modelling the Reynolds stresses in the continuous phase is based on a 2nd order closure technique, whereby turbulence is treated as anisotropic. In particular, the elliptic blending Reynolds stress model (EBRSM) is employed for the transport of the turbulent stresses. This method adopts Durbin's concept of elliptic relaxation for the integration of near-wall turbulence (Durbin, 1993). To this purpose, an elliptic function is incorporated for blending between an inhomogeneous near-wall pressure–strain tensor and a conventional homogeneous quadratic form for the outer region (Manceau and Hanjalic, 2000). For bubbly channel flows the modelling of turbulent wall effects by means of the pressure redistribution terms in RSM is relevant, since bubbles have low inertia and are therefore highly responsive to normal stresses developing near walls (Papoulias et al., 2016). Closure of the respective turbulent stresses of the dispersed phase (Eq. (3)) is provided by an empirical approach based on Issa's correlation (Gosman et al., 1992). This model assumes that the velocity fluctuations of the dispersed phase are directly linked to those of the continuous phase via a turbulent response function $f(\tau)$. This analogy is essentially derived from experimental data extrapolation, while also fitted with a correction for the volume-fraction loading. The general form reads as follows:

$$\boldsymbol{\tau}_i^n = \boldsymbol{u}_i' \boldsymbol{u}_i' = f(a_i) \boldsymbol{\tau}_{\mathrm{c}} \tag{7}$$

The continuity and momentum conservation equations of the dispersed phase (Eq. (1) and Eq. (2)) are augmented by an additional PBE for the number-density of the population (n_i):

$$\frac{\partial \overline{n}_i}{\partial t} + \nabla \cdot \langle n_i \boldsymbol{u}_i \rangle = \langle S_i \rangle \tag{8}$$

The RA convective term in Eq. (8) can be expressed as

$$\langle n_i \boldsymbol{u}_i \rangle = \overline{n}_i \langle \boldsymbol{u}_i \rangle + \langle n_i' \boldsymbol{u}_i' \rangle \tag{9}$$

Rearranging Eq. (2) and substituting in Eq. (9) provides the following relationship:

$$\langle n_i \boldsymbol{u}_i \rangle = \overline{n}_i \left(\langle \boldsymbol{u}_i \rangle_i - \frac{\langle \alpha_i \boldsymbol{u}_i' \rangle}{\overline{\alpha}_i} \right) + \langle n_i' \boldsymbol{u}_i' \rangle \tag{10}$$

The covariance products appearing in Eq. (10) can be modelled using the gradient closure hypothesis. Eq. (10) and Eq. (8) are combined to yield the RA transport equation for n_i:

$$\frac{\partial \overline{n}_i}{\partial t} + \nabla \cdot \overline{n}_i \left[\langle \boldsymbol{u}_i \rangle_i + D_T \nabla \left(\ln \overline{\alpha}_i - \ln \overline{n}_i \right) \right] = \langle S_i \rangle \tag{11}$$

The modelled part of the convective term which is expressed in logarithm form resembles the diffusive fluxes in typical transport equations. Despite that this term is not representing a physical process for the number-density property, and is in fact vanishing for homogeneous flows, it remains still essential for the numerical treatment of spurious dissipation attributed to the DQMoM method (Fox, 2003). The source-term S_i which is added to the right side of the number-density balance (Eq. (11)) encapsulates the growth or decline of the bubble population due to break-up and coalescences effects, respectively.

The utilized kernel for the break-up of bubbles is formulated by an empirical model (Tsouris and Tavlarides, 1994). According to this phenomenological approach, bubble break-up events are postulated as an ensemble probability product between the frequency of eddy-particle collisions ($h(d_i)$) and the energy that is required in order to rupture the surface of the entrained bubble. Based on the kinetic theory of gases and that the energy spectrum of eddies in the inertial subrange (Batchelor, 1970), the phenomenological break-up rate ($g(d_i)$) model is expressed as an exponential function of the Weber number (We):

$$g_B(d_i) = h(d_i) \cdot C_B \frac{(\varepsilon_c d_i)^{1/3}}{d_i} e^{-We_{cr.}/We} \tag{12}$$

where C_B is an empirical constant, ε is the turbulent dissipation, d_i is the bubble diameter, and $We_{cr.}$ denotes the critical Weber number. The probability density function of the newly created daughter bubbles assumes a normal distribution, which is linearly dependent on the surface energy required for the formation of a binary set of particles. The size of the resulting bubbles is determined by the minimum energy needed for a break-up event to occur, which generally leads to a pair consisting of a smaller and a larger particle.

Likewise, bubble coalescence events are modeled by an empirical model that assumes different physical processes during the mutual interaction of bubbles (Luo, 1993). According to this theoretical approach, colliding bubbles form a thin cushion of fluid-film between their contacting surfaces, which prevents the particles from merging unless gradually drained to a critical thickness. The efficiency of the process is described as a function of the colliding frequency and the time available for interacting, relative to the shrinkage rate of the thin-film. The collision frequency of bubbles is approximated in a similar way to the eddy–particle collisions, assuming that bubbles in turbulent flows behave like ideal gas molecules. The time particles spend in contact ($t_{cont.}$) is presumed to be directly proportional to the characteristic life span of eddies of similar size (Levich, 1962). An expression for the interaction time ($t_{int.}$) is derived by transforming the force balance of colliding particles into a film-thinning equation, which can be analytically integrated by imposing appropriate boundary conditions (Chesters, 1991). Based on the theory of the parallel-film model, the coalescence kernel is formulated as

$$g_C(d_i) = h(d_i, d_j) \cdot e^{C_C \cdot (-t_{cont.}/t_{int.})} \tag{13}$$

where C_C in Eq. (13) is a calibration constant.

The solution of the number-density and volume-fraction PBE is sufficient for calculating an equivalent diameter—the volume-mean—for each of the dispersed bubble groups:

$$d_i = \sqrt[3]{6\overline{\alpha}_i / (\pi \overline{n}_i)} \tag{14}$$

3 Polydispersed simulations in bubbly channel flows

Coalescence and break-up models for simulating BSD in multiphase flows involve a number of empirical constants which require a priori calibration (i.e., C_B in Eq. (12) and C_C in Eq. (13)). To this purpose, in the present work parametric calculations are performed for tuning as well as validating the A-MuSiG model based on three experiments in fully-developed turbulent bubbly flows: (i) a pipe flow under microgravity conditions (Section 3.1), (ii) a horizontal channel flow (Section 3.2), and (iii) a vertical flow past an obstacle (Section 3.3). The analysis of each case study including specifics regarding the experiments, simulation conditions, and predicted results, is presented in the upcoming dedicated sections.

Typical integral quantities that are utilized for the assessment of the results, in particular the mean particle sizes, are purposely introduced prior to the forthcoming analysis. These expressions are derived by averaging the BSD output from the A-MuSiG model, against different weighting functions of the moments. The resulting mean bubble diameters can be encapsulated in a generic formula:

$$d_{pq} = \sqrt[(p-q)]{\sum n_i d_i^p \,/\, \sum n_i d_i^q} \tag{15}$$

where p and q are integer indexes that synthesize different types of mean diameters. The most commonly used definitions include the arithmetic mean diameter d_{10}:

$$d_{10} = \sqrt{\sum n_i d_i / \sum n_i} \tag{16}$$

the surface mean, commonly known as Sauter mean diameter d_{32}:

$$d_{32} = \sqrt{\sum n_i d_i^3 / \sum n_i d_i^2} \tag{17}$$

and the volumetric mean diameter d_{30}:

$$d_{30} = \sqrt{\sum n_i d_i^3 / \sum n_i} \tag{18}$$

3.1 Bubbly pipe flow in microgravity conditions

The lifetime of travelling bubbles is mostly dependent on the available surface-energy of the interface as well as the conditions encountered along the flow. Strong turbulent disturbances and hydrodynamic interactions are amongst the principal physical mechanisms mentioned in the literature, which gradually result in bubble deformation and break-up when the restoring interfacial forces are exceeded. If the dominant break-up mechanisms are suppressed—by reducing turbulence in the flow and relaxing the forces acting on the interface—then the life expectancy of bubbles can be extended. Such conditions are emulated in microgravity experiments on bubbly pipe flow, for low Reynolds numbers and dilute mixtures (Kamp et al., 2001). In such experimental arrangement, buoyancy forcing effects relating to slip-induced drag and turbulence generation at the trailing wakes of bubbles are minimized and thus a hydrodynamic equilibrium state between the liquid and dispersed phases is promoted. Under these conditions the population sizes and number-density of the dispersed bubbles are mainly governed by coalescence events, depending on the probability of interparticle collisions and interaction time.

Table 1 describes the experimental flow conditions selected for modelling bubble coalescence effects with the A-MuSiG model, in terms of the superficial liquid (j_L) and gas velocities (j_G), the bubble volume-fraction (α_d) as well as the operating Re number. The Perspex pipe utilized in these experiments measured 4 m in length and 40 mm in diameter. BSD measurements were acquired at a downstream location (~0.5–0.7 m) where the two-phase flow is fully developed, using a synchronized dual system of high-speed cameras. The Sauter mean diameter (d_{32}) at the inlet and outlet of the channel were approximated using an image post-processing algorithm (Table 2).

The flow conditions listed in Tables 1 and 2 are simulated with the two-fluid A-MuSiG model in order to reproduce the BSD as reported in the experiments. The flow domain for these simulations is modeled as two-dimensional axisymmetric and is discretized by 16,000 uniform quadrilateral elements (Fig. 1). At the inlet boundary the assigned velocity (U) and turbulence (k and ε) profiles are provided by corresponding fully-developed single-phase calculations. The initial sizes of the introduced bubbles are represented by a log-normal distribution, with mean and variance both determined by the available experimental measurements. For the discretization of the BSD the dispersed phase-space is partitioned into five size-groups.

The two-fluid A-MuSiG set-up is complemented with the previously described turbulent collision and coalescence models (Eq. (13)). In order to calibrate the contribution of the empirical input (C_C) in the overall efficiency of the process different values are tested (Table 3), in the range of 1.0 to 2.5. In these parametric runs break-up effects are neglected.

Table 1 Experimental conditions of microgravity channel flow

Experiment No.	j_L (m/s)	j_G (m/s)	α_d (—)	Re
1 (D21)	1.558	0.061	0.0286	69244
2 (E16)	0.954	0.128	0.0912	42400
3 (E17)	0.937	0.219	0.15	41644
4 (I18)	0.842	0.223	0.17	37422

Table 2 Sauter mean diameter measurements at the inlet and outlet of the channel

Experiment run	d_{32} (mm), inlet	d_{32} (mm), outlet
1 (D21)	2.67	5.02
2 (E16)	5.07	12.94
3 (E17)	5.79	16.18
4 (I18)	4.02	14.07

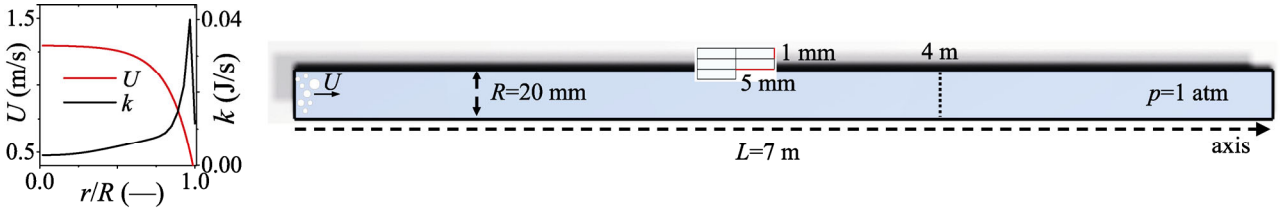

Fig. 1 Physical flow domain and boundary conditions for pipe flow in microgravity.

Table 3 A-MuSiG parametric coalescence simulations in microgravity bubbly flow

Run	Collision model	Coalescence model	Efficiency const. C_C
1 (D21) 2 (E16) 3 (E17) 4 (I18)	Turbulent & Zaichik	Luo & Film-Drainage	1.0–2.5

The mean flow characteristics and bubble coalescence behavior in the tested parametric simulations are similar. Indicative results for a typical scenario (I18) are presented in Fig. 2, in terms of the bubble volume-fraction, number-density as well as coalescence rate (CR). As shown in the illustrated predictions, due to the absence of gravity the bubbly flow retains a uniform distribution inside the pipe, while the population number-density gradually declines due to coalescence. Despite the fact that interparticle collisions are more frequent as the bubbles merge and grow in size, the probability of coalescence is steadily reduced during the journey along the channel. This implies that the fluid-film separating large bubbles in contact is substantially thick and the available interaction time is not sufficient for drainage, what prohibits coalescence.

The induced coalescence effects on the development of the population inside the channel can be evaluated in a quantitative manner by plotting the number-density and sizes of the individual bubble groups, along the axis of symmetry (Fig. 3).

The population number-density and group-sizes plotted in Fig. 3 correspond to different discretization classes for the moments of the dispersed bubbles, with G0 and G4 denoting the smallest and largest size-groups in the BSD respectively. As shown in these graphs, the endured coalescence events along the pipe are forcing the individual bubble groups to an asymptotic growth in terms of their sizes and an analogous exponential decay with respect to their population numbers.

Variations in the properties of the dispersed bubble population are interlinked to the developing hydrodynamic interactions, which in turn are responsible for regulating the momentum exchange between the flow phases. The resultant flow velocity when the phases reach equilibrium will depend on the interfacial area, and therefore the properties of the bubble population. Therefore, by comparing measurements of the pressure-drop across the channel against respective predictions (Fig. 4), it is possible to get an initial indication of whether the modelled bubble population is representative of the experiments. In that respect, the performed parametric runs exhibit negligible differences relative to the measurements, less than 3%, which implies that the modelled population sizes and numbers are comparable to those measured in the experiments.

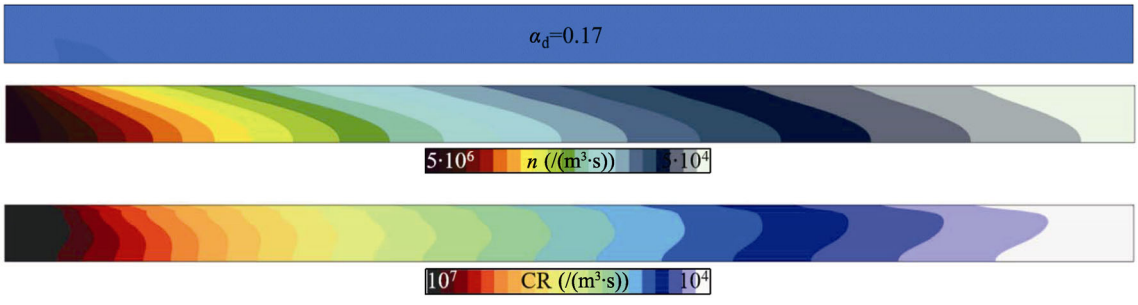

Fig. 2 Predicted distributions for the volume-fraction, number-density and coalescence rates for Run I18.

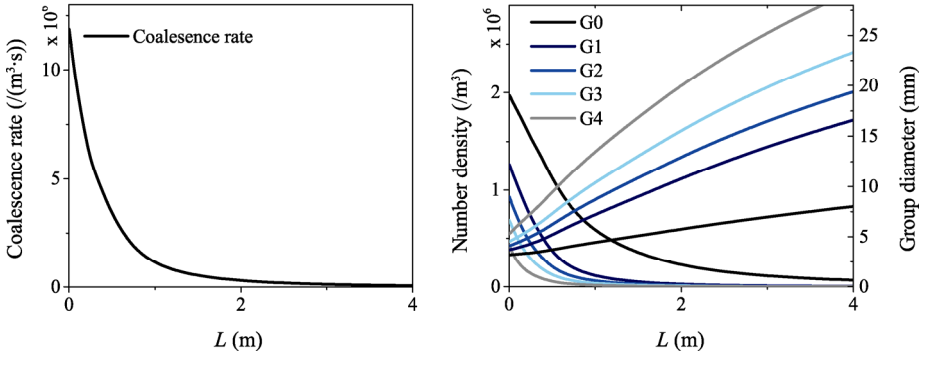

Fig. 3 Predicted bubble coalescence rate, number-density, and group-size variations along the axis-symmetry boundary for I18 run.

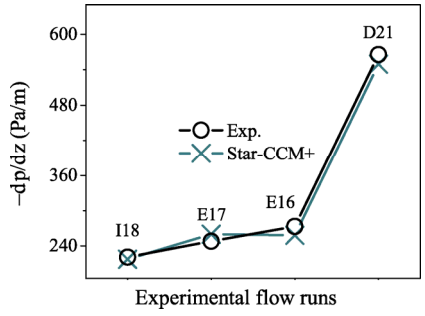

Fig. 4 Model predictions and experimental measurement (Kamp et al., 2001) for the pressure-drop along the pipe.

The sensitivity of the calculated bubble mean sizes for the tested coalescence kernels and empirical constants is reflected on the predictions presented in Fig. 5. The scatter symbols in these graphs are averaged measurements of the bubble sizes—defined in terms of the d_{10}, d_{32}, and d_{30} mean diameters—acquired at the inlet and outlet of the experimental pipe. The spatial distribution line plots represent the corresponding A-MuSiG parametric calculations (Table 3), along the axis of the pipe; each tested combination for modelling bubble coalescence and turbulent collisions is denoted by a different color, while solid and dash lines are adopted for distinguishing between different values of the coalescence efficiency constant (C_C). According to these graphs, it is evident that the efficiency constant inherent to coalescence kernels requires a priori tuning in order to approach the bubble sizes indicated in the experiments. The emerging discrepancies in the modelled mean bubble sizes exhibit a tendency to increase as the concentration of the bubble population becomes high (i.e., E17 and I18 runs), irrespective of the models used. By means of an optimization study it is possible to calibrate C_C, to values that effectively minimize the modelling differences. For the considered pipe flows, limiting the coalescence efficiency by increasing C_C to values in the range of 1.7 to 2.5 seems to provide more accurate sizes for the resulting bubbles at the outlet. The effects of the particle collision rate $(h(d_i,d_j))$ in the coalescence process are shown in the calculations performed with the so-called film-drainage model (cyan and gray lines)—a generic exponential model of the form $\sim C_C \cdot e^{We^n/Re^m}$, where n and m are scaling constants. The collision model is formulated in the work of Zaichik et al. (2010), which can be considered as an extension to the turbulent collision kernel since it also accounts for inertial effects that are appreciable in flows with high particle-to-fluid density ratio. The predicted bubble sizes when using the aforementioned kernels for modeling coalescence effects seem to be increasing at a faster rate upstream of the channel, while downstream the growth slope gradually becomes asymptotic. Overall, the results obtained by the tested phenomenological turbulent coalescence kernels seem to converge to similar solutions for the mean sizes of the bubbles, provided that the efficiency of the modeled coalescence process is properly scaled.

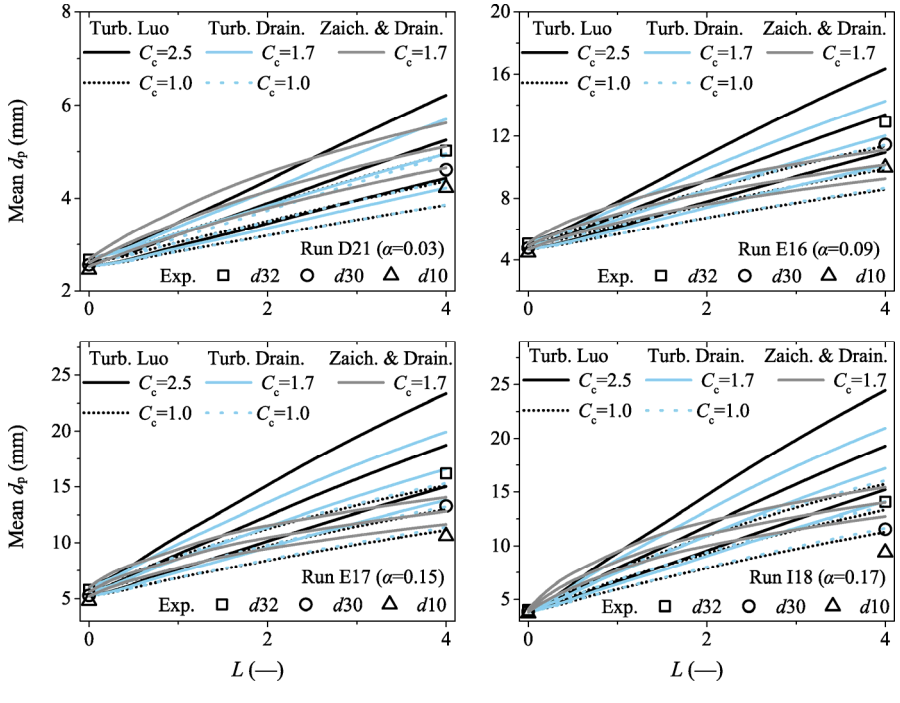

Fig. 5 A-MuSiG model predictions and experimental measurements (Kamp et al., 2001) of the bubble mean diameters across the channel.

The examined two-phase channel flow experiments provided the necessary size distribution data for tuning the coalescence efficiency of bubbles, assuming that break-up effects are suppressed due to the microgravity conditions. In the next section, the calibrated A-MuSiG approach for the coalescence of bubbles is also integrated with *Tsouris* and *Tavlarides* turbulent break-up model (Eq. (12)), in order to evaluate the combined effect in bubbly flows developing in a horizontal pipe.

3.2 Bubbly flow in horizontal pipe

The experimental results utilized for the second part of the A-MuSiG validation analysis consist of bubbly flow distributions in horizontal pipe flows (Kocamustafaogullari and Wang, 1991), where buoyancy forcing effects have a significant impact on the population dynamics. In these experiments, a closed-loop rig is equipped with a transparent glass pipe 14 m in length and 50 mm in diameter, where gravity acts along the normal direction of the flow. Air bubbles are introduced upstream of the water flow through a porous medium chamber, with representative pore sizes of 1 mm. The two-phase flow is allowed to develop and mix along the pipe, before coming in contact with a dual-sensor installed at the center of the test-section (~7 m) which probes the spatial distribution of the bubbly phase. In principle, the utilized electrical resistivity sensors provide instantaneous voltage signals that fluctuate depending on the material in contact; when the wire probe is insulated by a crossing bubble the electric circuit is closed, while when the resistance is immersed in water most of the electricity is conducted through the medium (Hampel, 2019). The acquired electrical signals are averaged over a sufficient period of time and converted into meaningful bubble characteristics (i.e., bubble sizes, population concentration, and velocities) by means of a post-processing algorithm. Using this experimental arrangement, the phase distribution of the bubbly flow is characterized for different *Re* numbers, bubble volume-fractions, and superficial phase flow-rates. The particular flow conditions selected for validating the A-MuSiG model are described in Table 4.

Similarly to the previously presented calculations (Section 3.1), also in this case the performed simulations consider different superficial flow velocities and loading fractions for the dispersed phase. The workflow and model set-up for the current two-phase flow simulations are adopted from the practices developed during the previous analysis. Accordingly, the same dispersed bubble forces are assumed for coupling the two phases and likewise, fully-developed flow profiles for the velocity and turbulence are assigned as inlet boundary conditions. Since the flow is not favored by any preferential symmetry, a three-dimensional computational domain is constructed for the discretization of the pipe channel consisting of approximately 950,000 quadrilateral elements (Fig. 6). The initial bubble sizes at the inlet are defined based on the equivalent porosity size (i.e., 1 mm) of the porous media chamber, where the dispersed phase is introduced into the flow.

The migration trajectory of bubbles in channel flows, and thereby the phase distribution, are determined by the acting forces which to a degree are also influenced by the developing turbulent field. Therefore, bubbles with different sizes will reside in different parts of the flow in order to coexist in equilibrium with their surroundings, depending also on the volumetric flow-rate of each phase. In order to investigate the hydrodynamic behavior of bubbles in the considered channel flow, different momentum closure models are tested for the flow forces as well as the turbulent stresses. To this purpose, the standard two-equation k–ε model is used, while calculations are also performed using second-moment closures based on RSM. In the latter class of anisotropic models, two alternative techniques are evaluated for modelling the pressure-strain term; a typical linear model (Gibson and Launder, 1978) and the elliptic relaxation approach (Manceau and Hanjalic, 2000). With regards to sub-grid processes which operate on the size and number-density of the population, the A-MuSiG calculations account for the birth and death rates of bubbles due to turbulent breakage (Eq. (12)), in addition to the calibrated *Luo* kernel for modelling coalescence effects (Eq. (13)). The break-up kernel requires a user input for the particle's $We_{cr.}$, which for

Table 4 Experimental conditions of horizontal bubbly flow

Experiment No.	j_L (m/s)	j_G (m/s)	α (—)	*Re*
1 (19)	5.10	0.24	0.0434	
2 (20)	5.10	0.44	0.0802	~280000
3 (22)	4.98	0.88	0.204	

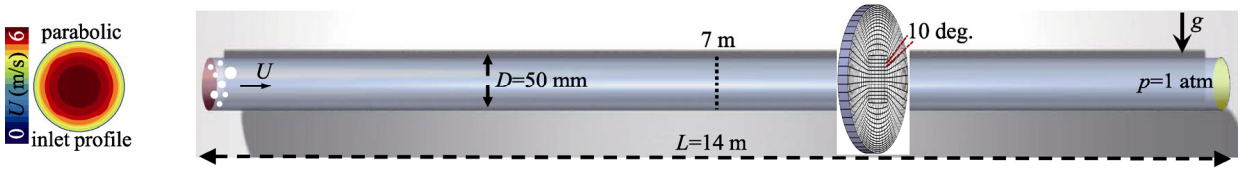

Fig. 6 Physical flow domain and boundary conditions for the horizontal pipe flow.

bubbles typically ranges between 0.5 and 3.0 depending also on the material properties of the background flow (Hinze, 1955; Hesketh et al., 1987). In detail, the performed parametric A-MuSiG simulations are summarized in Table 5.

The development of the bubbly channel flow for a particular parametric condition (Run 20) is illustrated in Fig. 7, in terms of the predicted bubble volume-fraction distribution, number-density, coalescence rate as well as break-up rate (BR). As expected for this scenario, the hydrodynamic behavior of the bubble population along the horizontal channel flow is mainly dominated by buoyancy effects. Under the influence of gravity, bubbles seem to gradually separate from the heavier carrier phase and accumulate near the upper wall of the pipe. The high population density forming at the top of the pipe encourages closely clustered bubbles to collide and stay in contact long enough to coalesce. Growing bubbles due to coalescence are more susceptible to break-up, as the restoring surface-tension force becomes insignificant compared to the destructive energy of eddies dissipating near wall boundaries. The final size of bubbles is gradually adjusted to the local flow conditions, in favor of a balance between the competing break-up and coalescence mechanisms. For the current flow conditions coalescence events appear to be dominant over break-up effects, implying that buoyancy forcing and turbulent fluctuations are not as effective as the interparticle collisions in changing the bubble sizes and population density.

The predicted spatial distributions of the bubble Sauter mean diameter (d_{32}) and volume-fraction for the tested horizontal channel flows are plotted in Fig. 8. Each individual line in these graphs corresponds to a different parametric calculation (Table 5), while the scatter circle symbols represent the available experimental measurements for the examined cases. The plotted spatial flow profiles consist of data extracted from the median vertical distance between the bottom and top walls (r/R= −1.0 to 1.0), which is part of the downstream cross-section (X = 7 m) probed with the wire-mesh sensor.

As previously shown in Fig. 6, the bubble population in the horizontal channel flow accumulates at a concentration site near the turbulent boundary layer developing at the top wall. However, the resulting volume-fraction peak of the bubble population near the top wall appears exaggerated by the majority of the tested turbulence models. To a certain degree, this effect is less pronounced when using second-moment closures. Likewise, the radial distribution of the mean bubble sizes is better predicted assuming the RSM, contrary to the isotropic k–ε which results into underestimation of the developing sizes. In fact, it seems that the two-equation turbulence model is not adequately representing the interaction length-scales and mixing flow characteristics, in order to sustain the underlying modelled break-up and coalescence mechanisms.

The effects of different turbulence and force closures on the internal properties of the bubble population become more evident if the characteristics of the developing dispersed regime are inspected across the entire cross-section of the channel (Fig. 9) where measurements are acquired. To a certain degree, the excess of bubbles predicted near the top wall seems to be limited when accounting for the wall-reflection terms in the LRSM approach. The extra correction terms for modeling wall effects are effectively realized as additional normal stresses that diminish the wall-normal components in favor of the streamwise and spanwise direction (Launder and Sandham, 2002). Likewise, the turbophoresis force is

Table 5 A-MuSiG parametric coalescence and break-up simulations in horizontal bubbly flows

	Fluid solver	Bubble interaction models			
Run	Turbulence model	Collision rate model	Coalescence model	Break-up model	Forces
1 (19) 2 (20) 3 (22)	k–ε LRSM EBRSM	Turbulent	*Luo* (C_C = 2.5)	*Tsouris & Tavlarides* ($We_{cr.}$ = 0.5)	F_{CD}, F_{VM}, F_{TD}, F_T

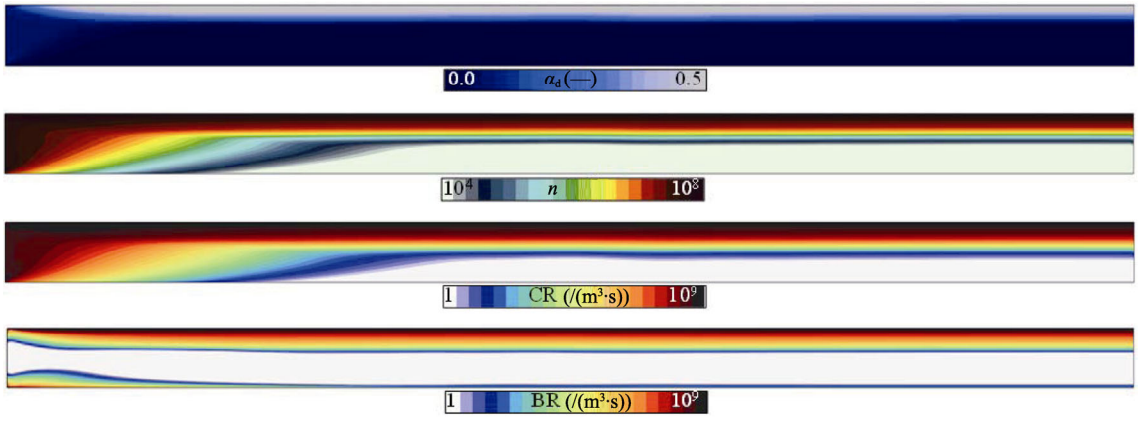

Fig. 7 Predicted distributions for the volume-fraction, number-density, coalescence and break-up rates for Run 20.

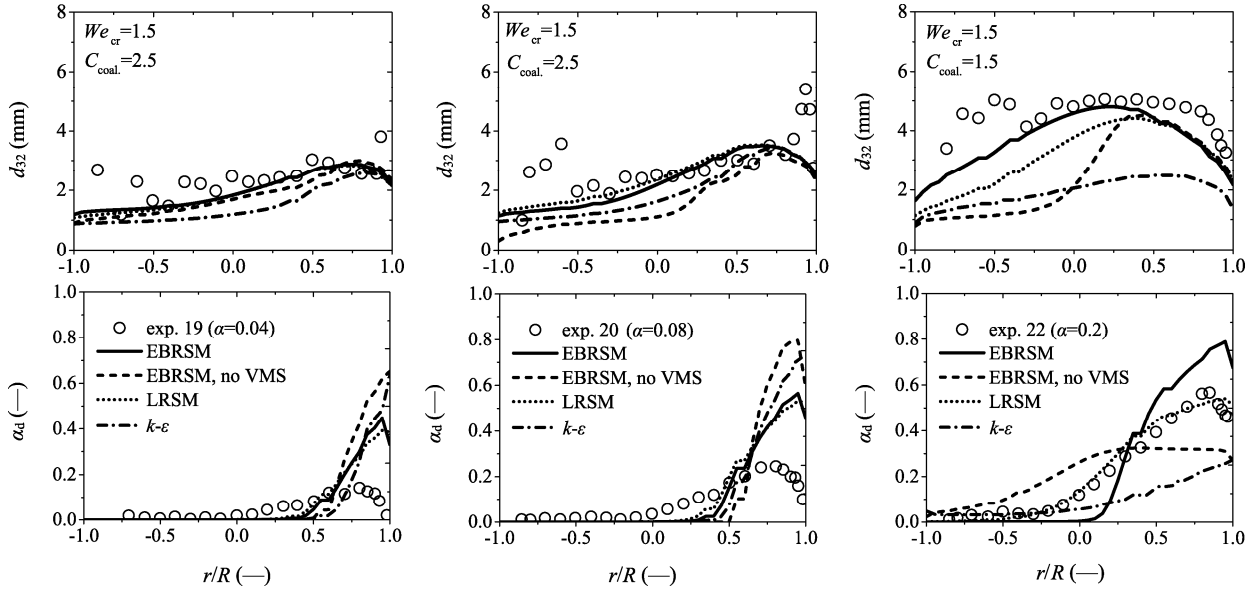

Fig. 8 A-MuSiG model predictions and experimental measurements (Kocamustafaogullari and Wang, 1991) for the spatial distributions of the bubble Sauter mean diameter (d_{32}) and bubble volume-fraction; the flow profiles are plotted across the vertical diameter at a downstream cross-sectional plane (X = 7 m).

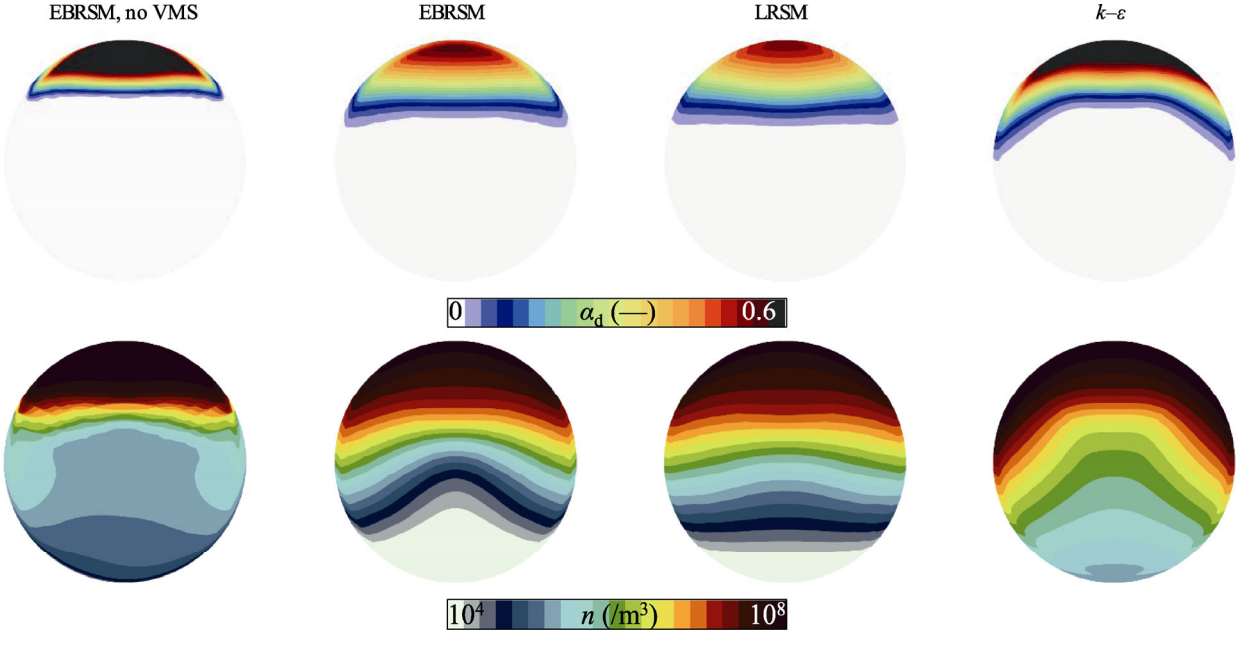

Fig. 9 Predicted mean volume-fraction and logarithmic number-density distributions across the vertical measurement plane (X = 7 m) of the horizontal channel flow (Run 22).

acting to redistribute the population of bubbles towards areas exhibiting high production of turbulent kinetic energy, which for pipe flows develop near the wall and in particular close to the outer region of the boundary layer (Young and Leeming, 1997). Therefore, despite that in certain cases low-order turbulence models combined with the most essential force closures (e.g., drag, lift, and turbulent dispersion) may be adequate for predicting the mean behavior of dispersed phase flows, neglecting the three-dimensional character of Reynolds stresses and induced turbulent-drift effects due to turbophoresis appear to have a considerable impact on the mixing behavior as well as coalescence and break-up of the bubble population. Since the momentum and population balances are coupled via the group-sizes, the aforementioned closures are also affecting the prediction of the local bubble sizes.

The last two sections in this study presented a parametric analysis of different bubbly regimes in channel flows for

numerous operating conditions, with the objective to calibrate empirical constants involved in modelling coalescence and break-up effects according to experimental measurements. In the forthcoming section, the A-MuSiG model and optimized empirical kernels from the preceding analysis are evaluated against an additional bubbly flow experiment conducted in an obstructed channel.

3.3 Bubbly flow in vertical obstacle channel

In this section the calibrated A-MuSiG model is validated against reported experiments in two-phase channel flows, conducted in TOPFLOW facilities (Krepper et al., 2009). The vertical channel utilized in these experiments is made of Perspex plastic and measures 0.2 m in diameter and 9 m in length (DN200). Water is pumped at different flow-rates inside the pipe circuit, while bubbles are introduced using a sparger system—consisting of 16 radial tubes, with multiple injection port 0.8 mm in diameter—mounted on the central axis of the channel close to the entry. The bubbly flow is allowed to develop undisturbed for most of the part of the channel (~5.5 m), prior to entering the test-section which is fitted with a half-moon shaped obstacle blocking half of the available flow area. Wire mesh sensors are installed at different axial locations downstream and upstream of the obstacle wall for measuring properties of the bubble population such as velocity, size, and number-density. Two experimental scenarios are considered for the current validation analysis; in both cases the laboratory circuit is maintained at standard pressure (1 atm) and temperature (23 °C) conditions, while the superficial fluxes for the flow phases varied within the bounds of the bubbly regimes. In detail, the considered flow conditions are summarized in Table 6.

The solution domain for simulating the development of the dispersed bubbly flow across the obstructed vertical pipe covers the test-section part of the channel (~3 m), assuming a symmetry boundary along the mid-plane. For the spatial discretization approximately 1.1 million grid elements are used, consisting of mixed quadrilaterals and wall prism-layer cells. At the inlet boundary fully-developed profiles for the velocity and turbulence properties are prescribed. The mean size ($\overline{d}$) and variance (σ) of the bubbly distribution assigned at the inlet boundary are taken from measurements acquired 0.52 m upstream of the half-moon obstacle. The physical flow boundaries and the grid resolution in the vicinity of the obstacle wall are illustrated in Fig. 10. The outlined cross-sections along the channel correspond to some of the locations selected for data acquisition by adjusting the movable wire-mesh sensor.

The adopted closures for modelling turbulence as well as simulating bubble sub-grid break-up and coalescence effects are deduced from the previously conducted parametric flow simulations (Sections 3.1 and 3.2). In the current analysis, different modelling assumptions for the discretization of the polydispersed phase-space are evaluated in the context of the A-MuSiG approach. To this purpose, the multi-speed as well as single-speed mode of the A-MuSiG model are examined, assuming a discrete momentum balance for each of the size-groups or a collective velocity field for the entire population, respectively. In addition, different number of size-groups are used for adaptively discretizing the BSD, ranging from 5 to 15. A brief description of the considered parametric simulations is provided in Table 7.

The development of the multiphase flow-field behind the obstacle wall can be visualized by plotting the mean streamlines and the volume-fraction distribution of the predicted bubble population (Fig. 11). As can be seen, the obstacle wall that is positioned at right angles against the flow is generating a strong vortex wake downstream of the

Table 6 Experimental flow conditions of obstacle bubbly flow

Experiment No.	j_L (m/s)	j_G (m/s)	α (—)	*Re*
Run 074 (1)	1.017	0.0386	0.0231	~260000
Run 096 (2)	1.017	0.0898	0.0565	

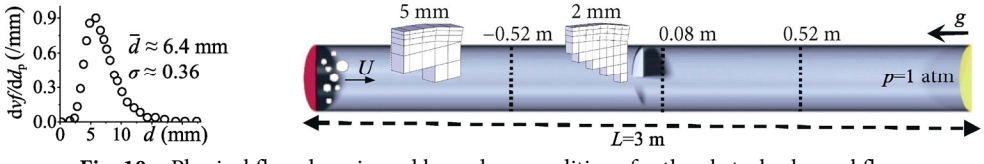

Fig. 10 Physical flow domain and boundary conditions for the obstacle channel flow.

Table 7 A-MuSiG parametric bubbly flow simulations in obstacle channel

Fluid solver		A-MuSiG solver		Bubble interaction models		
Run	Turbulence model	Bubble velocity	Number of size-groups	Collision rate model	Coalescence model	Break-up model
1 2	EBRSM	single-speed & multi-speed	5, 9, 15	Turbulent	Luo (C_C = 2.5)	Tsouris & Tavlarides (We_{cr} = 0.5)

channel, which occupies the space behind the obstruction. The adverse pressure-gradient that develops behind the obstacle due to flow separation attracts the travelling bubbles towards the wake region. A large majority of the population is trapped inside the vortex core, while bubbles that seem to escape are carried along the detached shear-layer forming downstream of the sharp edges of the obstacle wall.

A quantitative comparison of the predicted bubbly flow characteristics against the experimental measurements is provided for the first test case (Run 074), in terms of the spatial velocity and volume-fraction distributions developing at different elevation planes along the pipe (Fig. 12). The bubble concentration is presented in normalized form ($\widetilde{vf}$), relative to the local cross-sectional averaged volume-fraction (Frank et al., 2007). The flow profiles are plotted across the median line of the measurement planes which lies on the symmetry boundary, covering the distance between the walls. The position of the half-moon obstacle relative to the vertical walls is located at the right part of the pipe (i.e., r/R = 0.0–1.0). Overall, the predicted mean flow characteristics appear to be aligning well with the corresponding spatial measurements. Discrepancies are mainly noticed downstream of the obstacle, at the space inhabited by the separated wake. In particular, the intensity of the detached vortex seems to be overpredicted, especially near the sharp edges of the obstacle (X = 0.08 m, X = 0.25 m for r/R = 0.0–1.0). As a result, the mixing between the separated and unrestricted parts of the flow downstream of the pipe appears to be less diffused compared to the experiment (X = 0.25 m for r/R = −1.0–0.0). To a certain degree, the observed differences in the mean flow velocity are also affecting the local distribution of the bubbles. Most likely, a factor that contributes to the observed differences is the three-dimensional character of the vertical flow and the turbulent mixing behavior, which to an extent are both compromised as a consequence of the symmetry assumption along the central plane of the pipe.

The rate of bubble coalescence and break-up events across the pipe depends on the local flow conditions and in particular the characteristics of the forming turbulent structures (Fig. 13). Areas where break-up effects appear to be dominant are established in places where strong interactions between eddies and bubbles are occurring; these zones are mostly developing along the separated turbulent-layer, which is initiated around the sharp periphery of the flow facing obstacle and extends further downstream as part of the wake. The region behind the obstacle is occupied by a

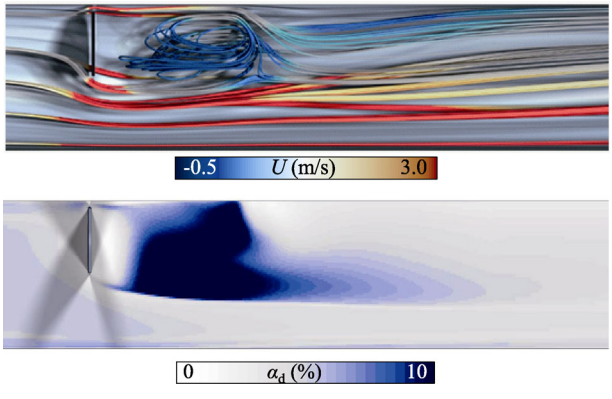

Fig. 11 Predicted flow streamlines and bubble volume-fraction distribution behind the obstacle (Run 096).

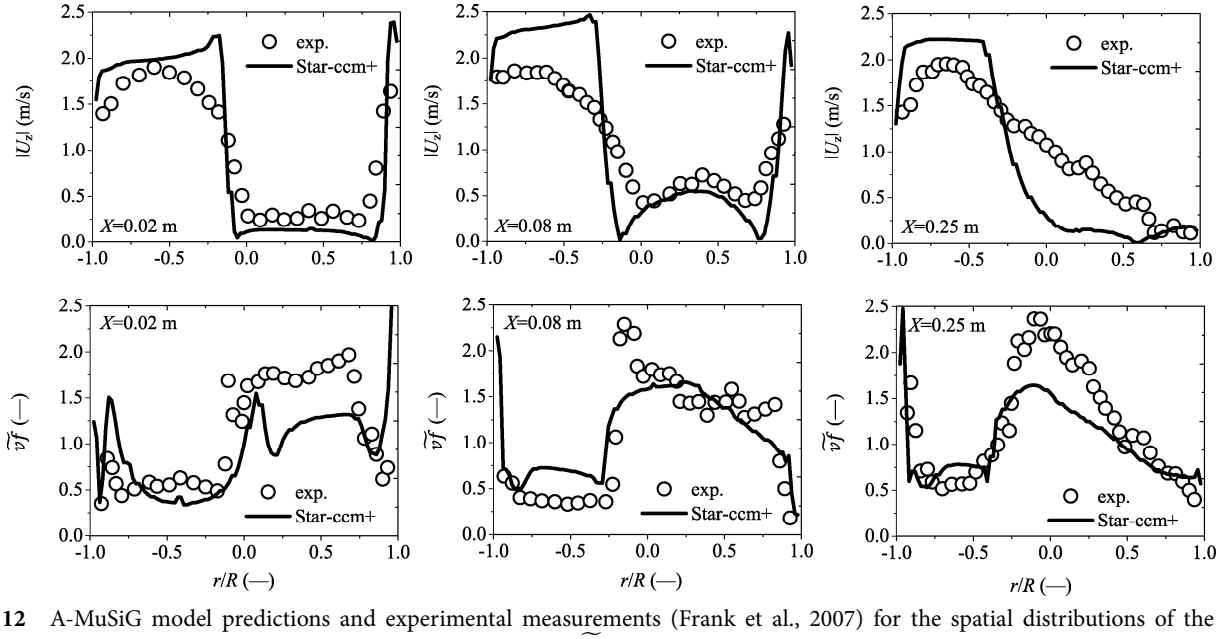

Fig. 12 A-MuSiG model predictions and experimental measurements (Frank et al., 2007) for the spatial distributions of the axial velocity magnitude $|U_z|$ and normalized bubble volume-fraction ($\widetilde{vf}$) at different elevation planes (Run 074).

vortex structure which continuously mixes the entrapped bubbly population inside the confined space of the wake. The resulting flow conditions at the vicinity of the vortex are favorable for frequent bubble–bubble collisions and persistent interactions, both leading to high coalescence rates.

The bubble size distribution across the channel is adjusted to the developing coalescence and break-up rates, correlating to the local flow conditions. The evolution of the characteristic bubble sizes is demonstrated by means of the predicted PDF (Fig. 14), which represents averaged population clusters at the flow planes surveyed by the wire-mesh sensors. The individual line plots on these graphs refer to calculations with different number of size-groups. Upstream of the wake (X = 0.08 m), the peak of the PDF distribution seems to be shifted towards larger bubble sizes implying that coalescence effects are dominant in this part of the flow. The enhanced mixing between eddies and bubbles downstream of the vortex wake (X = 0.52 m) encourages break-up effects, which gradually diminish the size and variance of the population. Overall, the A-MuSiG predictions appear to be independent of the number of size-groups used for discretizing the phase-space.

The solution effects attributed to the momentum closure assumption for modelling bubble–flow interactions (i.e., single-speed or multi-speed velocity fields) are interpreted in terms of the cumulative distribution function (CDF) (Fig. 15), which is integrated from the previously presented PDF distributions. Accounting only for mean size bubble interactions with the flow by adopting a single velocity-field for the entire dispersed phase population, seems to result into overestimation of the BSD developing behind the obstacle (X = 0.08 m), especially in the mid-size range. The distribution discrepancies emerging near the obstacle of the pipe grow further downstream of the turbulent vortex flow (X = 0.52 m), after the bubbles have spend sufficient time interacting with the surrounding flow.

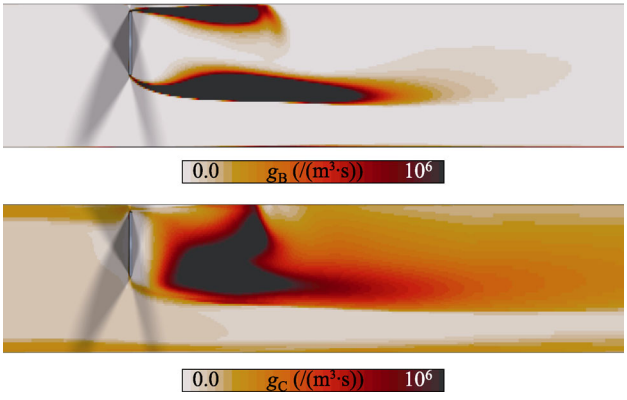

Fig. 13 Predicted bubble break-up and coalescence rates (Run 096).

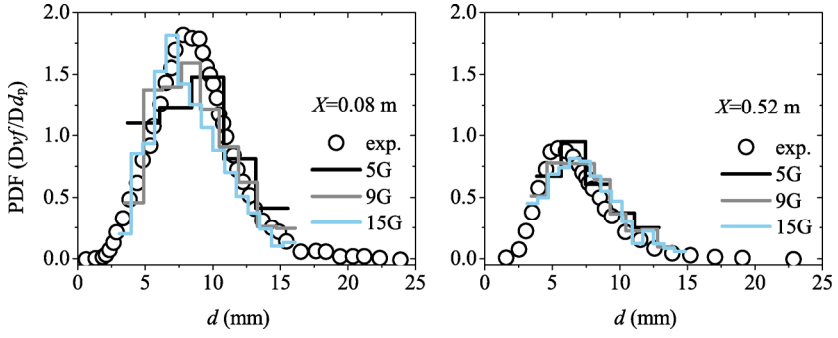

Fig. 14 A-MuSiG model predictions and measurements (Krepper et al., 2009) for the PDF of the bubble size distribution at 0.08 and 0.52 m planes (Run 096).

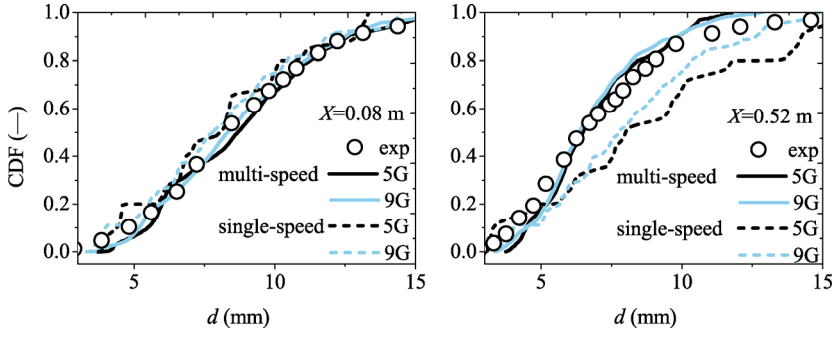

Fig. 15 A-MuSiG model predictions and measurements (Krepper et al., 2009) for the CDF of the bubble size distribution at 0.08 and 0.52 m planes (Run 096).

4 Conclusions

In the presented analysis the A-MuSiG model implemented in the Eulerian multiphase solver in Simcenter STAR-CCM+ is validated against numerous experiments in bubbly channel flows. The multiphase inspection techniques employed in the considered experiments provided essential sets of measurements that characterized the properties of the bubble population as well as mean flow for different operating conditions. The principal objective of the performed CFD investigation is aligned with a more general research effort towards the evaluation of the predictive capabilities of PBE methods as well as empirical kernels for modelling sub-grid coalescence and break-up mechanisms, which to a certain extent also pertains to the turbulent-stresses and forces closures adopted for the momentum equations. To this purpose, the conducted parametric simulations accounted for phenomenological models relating to a wide spectrum of particle physical processes, such as eddy–particle interactions, turbulent interparticle collisions and film-drainage effects between contacting interfaces, as well as anisotropic closures strategies and wall-reflection effects. The obtained predictions imply that to a degree, the empirical coalescence and break-up kernels can be calibrated to fit the population size distributions measured in the experiments, provided that the underlying turbulent length-scales of the carrier flow and momentum balance of the moving particles are adequately modeled. Uncoupling the instantaneous size interactions of individual bubble groups with the background flow and instead modelling mean size interactions by assuming a single-velocity field for the entire population, is justified only in limited cases where the properties of the particulate phase are ideally homogeneous. Given the multifaceted nature of polydispersed flows, the proposed adaptive phase-space discretization algorithm is an advantageous technique for solving PBEs, since it reduces the dependent variables of the problem by calculating the population size-groups, instead of a priori prescribing a fixed number of classes. RANS closures for modelling turbulent fluid-flow and particle dynamics combine first principles to describe microscopic and macroscopic physical processes and as such rely on experiments as well as direct numerical simulation in order to recover information that may be lost due to formulation assumptions. Overall, the derivation and calibration of phenomenological particle sub-grid models to characterize physics relating to a wide spectrum of scales are demanding tasks, currently challenged by deep learning and machine training algorithms (Ma et al., 2015).

References

Auton, T. R., Hunt, J. C. R., Prud'Homme, M. 1988. The force exerted on a body in inviscid unsteady non-uniform rotational flow. *J Fluid Mech*, 197: 241–257.

Bartsch, C., Wiedmeyer, V., Lakdawala, Z., Patterson, R. I. A., Voigt, A., Sundmacher, K., John, V. 2019. Stochastic-deterministic population balance modeling and simulation of a fluidized bed crystallizer experiment. *Chem Eng Sci*, 208: 115102.

Batchelor, G. K. 1970. *An Introduction to Fluid Dynamics*. Cambridge University Press.

Bhole, M. R., Joshi, J. B., Ramkrishna, D. 2008. CFD simulation of bubble columns incorporating population balance modeling. *Chem Eng Sci*, 63: 2267–2282.

Bird, G. A. 1976. *Molecular Gas Dynamic*. Oxford University Press.

Chesters, A. K. 1991. The modelling of coalescence processes in fluid-liquid dispersions: a review of current understanding. *Chem Eng Res Des*, 69: 259–270.

Durbin, P. A. 1993. A Reynolds stress model for near-wall turbulence. *J Fluid Mech*, 249: 465–498.

Fox, R. O. 2003. *Computational Models for Turbulent Reacting Flows*. Cambridge University Press.

Frank, T., Prasser, H. M., Beyer, M., Issa, S. Al. 2007. Gas–liquid flow around an obstacle in a vertical pipe - CFD simulation & comparison to experimental data. In: Proceedings of the International Conference on Multiphase Flow, 6: 1–14.

Frenklach, M. 2002. Method of moments with interpolative closure. *Chem Eng Sci*, 57: 2229–2239.

Gibson, M. M., Launder, B. E. 1978. Ground effects on pressure fluctuations in the atmospheric boundary layer. *J Fluid Mech*, 86: 491–511.

Gordon, R. G. 1968. Error bounds in equilibrium statistical mechanics. *J Math Phys*, 9: 655–663.

Gosman, A. D., Lekakou, C., Politis, S., Issa, R. I., Looney, M. K. 1992. Multidimensional modeling of turbulent two-phase flows in stirred vessels. *AIChE J*, 38: 1946–1956.

Hampel, U. 2019. Measurement techniques and experimental investigations for multiphase flows. In: Proceedings of the 17th Multiphase Flow Workshop - Conference and Short Course.

Hesketh, R. P., Fraser Russell, T. W., Etchells, A. W. 1987. Bubble size in horizontal pipelines. *AIChE J*, 33: 663–667.

Hinze, J. O. 1955. Fundamentals of the hydrodynamic mechanism of splitting in dispersion processes. *AIChE J*, 1: 289–295.

Hinze, J. O. 1959. *Turbulence*. Mc Graw-Hill Inc, USA.

Hao, X., Zhao, H., Xu, Z., Zheng, C. 2013. Population balance-Monte Carlo simulation for gas-particle synthesis of nanoparticles. *Aerosol Sci Tech*, 47: 1125–1133.

Kamp, A. M., Chesters, A. K., Colin, C., Fabre, J. 2001. Bubble coalescence in turbulent flows: A mechanistic model for turbulence-induced coalescence applied to microgravity bubbly pipe flow. *Int J Multiphase Flow*, 27: 1363–1396.

Kim, Y. P., Seinfeld, J. H. 1990. Simulation of multicomponent aerosol condensation by the moving sectional method. *J Colloid Interf Sci*, 135: 185–199.

Kocamustafaogullari, G., Ishii, M. 1995. Foundation of the interfacial area transport equation and its closure relations. *Int J Heat Mass Tran*, 38: 481–493.

Kocamustafaogullari, G., Wang, Z. 1991. An experimental study on

local interfacial parameters in a horizontal bubbly two-phase flow. *Int J Multiphase Flow*, 17: 553–572.

Krepper, E., Beyer, M., Frank, T., Lucas, D., Prasser, H. M. 2009. CFD modelling of polydispersed bubbly two-phase flow around an obstacle. *Nucl Eng Des*, 239: 2372–2381.

Kumar, S., Ramkrishna, D. 1996a. On the solution of population balance equations by discretization—I. A fixed pivot technique. *Chem Eng Sci*, 51: 1311–1332.

Kumar, S., Ramkrishna, D. 1996b. On the solution of population balance equations by discretization—II. A moving pivot technique. *Chem Eng Sci*, 51: 1333–1342.

Launder, B., Sandham, N. 2002. *Closure Strategies for Turbulent and Transitional Flows*. Cambridge University Press.

Lee, K. W., Chen, J., Gieseke, J. A. 1984. Log-normally preserving size distribution for Brownian coagulation in the free-molecule regime. *Aerosol Sci Tech*, 3: 53–62.

Levich, V. G. 1962. *Physichemical Hydrodynamics*. New Jersey: Prentice Hall, Engewood Cliffs.

Liao, Y., Lucas, D. 2010. A literature review on mechanisms and models for the coalescence process of fluid particles. *Chem Eng Sci*, 65: 2851–2864.

Lo, S., Zhang, D. 2009. Modelling of break-up and coalescence in bubbly two-phase flows. *J Comput Multiphase Flows*, 1: 23–38.

Luo, H. 1993. Coalescence, breakup and liquid circulation in bubble column reactors. Ph.D. Thesis. Norges Tekniske Hoegskole, Trondheim.

Ma, M., Lu, J., Tryggvason, G. 2015. Using statistical learning to close two-fluid multiphase flow equations for a simple bubbly system. *Phys Fluids*, 27: 092101.

Manceau, R., Hanjalic, K. 2000. A new form of the elliptic relaxation equation to account for wall effects in RANS modeling. *Phys Fluids*, 12: 2345–2351.

Marchisio, D. L., Fox, R. O. 2005. Solution of population balance equations using the direct quadrature method of moments. *J Aerosol Sci*, 36: 43–73.

Martinez-Bazan, C., Rodriguez-Rodriguez, J., Deane, G. B., Montañes, J. L., Lasheras, J. C. 2010. Considerations on bubble fragmentation models. *J Fluid Mech*, 661: 159–177.

McGraw, R. 1997. Description of aerosol dynamics by the quadrature method of moments. *Aerosol Sci Tech*, 27: 255–265.

Mohs, A. J., Bowman, F. M. 2011. Eliminating numerical artifacts when presenting moving center sectional aerosol size distributions. *Aerosol Air Qual Res*, 11: 21–30.

Papoulias, D., Spalwski, A., Vikhansky, A., Lo, S. 2016. Eulerian multiphase predictions of turbulent bubbly flow in a step-channel expansion. Int Conference Mult Flow, Firenze, Italy.

Ramkrishna, D. 2000. *Population Balances Theory and Applications to Particulate Systems in Engineering*. Academic Press.

Ramkrishna, D., Singh, M. R. 2014. Population balance modeling: Current status and future prospects. *Annu Rev Chem Biomol Eng*, 5: 123–146.

Randolph, A. D. 1964. A population balance for countable entities. *Can J Chem Eng*, 42: 280–281.

Randolph, A. D., Larson, M. A. 1971. *Theory of Particulate Processes: Analysis and Techniques of Continuous Crystallization*. New York: Academic.

Sajjadi, B., Raman, A. A. A., Ibrahim, S., Shah, R. 2012. Review on gas–liquid mixing analysis in multiscale stirred vessel using CFD. *Rev Chem Eng*, 28: 171–189.

Shu, C. C., Chatterjee, A., Hu, W. S., Ramkrishna, D. 2012. Modeling of gene regulatory processes by population-mediated signaling: New applications of population balances. *Chem Eng Sci*, 70: 188–199.

Tomiyama, A., Tamai, H., Zun, I., Hosokawa, S. 2002. Transverse migration of single bubbles in simple shear flows. *Chem Eng Sci*, 57: 1849–1858.

Tsouris, C., Tavlarides, L. L. 1994. Breakage and coalescence models for drops in turbulent dispersions. *AIChE J*, 40: 395–406.

Vikhansky, A. 2013. Direct quadrature spanning tree method for solution of the population balance equations. *J Aerosol Sci*, 55: 78–88.

Vikhansky, A. 2017. Combined Multifluid-Population Balance Method for Polydisperse Multiphase Flows. Progress in App CFD, Trondheim, Norway: 281–284.

Vikhansky, A., Splawski, A. 2015. Adaptive multiply size group method for CFD-population balance modelling of polydisperse flows. *Can J Chem Eng*, 93: 1327–1334.

Wang, K., Yu, S., Peng, W. 2019. Extended log-normal method of moments for solving the population balance equation for Brownian coagulation. *Aerosol Sci Tech*, 53: 332–343.

Young, J., Leeming, A. 1997. A theory of particle deposition in turbulent pipe flow. *J Fluid Mech*, 340: 129–159.

Zaichik, L. I., Simonin, O., Alipchenkov, V. M. 2010. Turbulent collision rates of arbitrary-density particles. *Int J Heat Mass Tran*, 53: 1613–1620.

Zhao, H., Maisels, A., Matsoukas, T., Zheng, C. 2007. Analysis of four Monte Carlo methods for the solution of population balances in dispersed systems. *Powder Technol*, 173: 38–50.